CM² MAGAZINE

第 30 期

南方科技大学海洋磁学中心主编

创刊词

海洋是生命的摇篮，是文明的纽带。地球上最早的生命诞生于海洋，海洋里的生命最终进化成了人类，人类的文化融合又通过海洋得以实现。人因海而兴。

人类对海洋的探索从未停止。从远古时代美丽的神话传说，到麦哲伦的全球航行，再到现代对大洋的科学钻探计划，海洋逐渐从人类敬畏崇拜幻想的精神寄托演变成可以开发利用与科学研究的客观存在。其中，上个世纪与太空探索同步发展的大洋科学钻探计划将人类对海洋的认知推向了崭新的纬度：深海（deep sea）与深时（deep time）。大洋钻探计划让人类知道，奔流不息的大海之下，埋藏的却是亿万年的地球历史。它们记录了地球板块的运动，从而使板块构造学说得到证实；它们记录了地球环境的演变，从而让古海洋学方兴未艾。

在探索海洋的悠久历史中，从大航海时代的导航，到大洋钻探计划中不可或缺的磁性地层学，磁学发挥了不可替代的作用。这不是偶然，因为从微观到宏观，磁性是最基本的物理属性之一，可以说，万物皆有磁性。基于课题组的学科背景和对海洋的理解，我们对海洋的探索以磁学为主要手段，海洋磁学中心因此而生。

海洋磁学中心，简称 CM^2，一为其全名“Centre for Marine Magnetism”的缩写，另者恰与爱因斯坦著名的质能方程 $E = MC^2$ 对称，借以表达我们对科学巨匠的敬仰和对科学的不懈追求。

然而科学从来不是单打独斗的产物。我们以磁学为研究海洋的主攻利器，但绝不仅限于磁学。凡与磁学相关的领域均是我们关注的重点。为了跟踪反映国内外地球科学特别是与磁学有关的地球科学领域的最新研究进展，海洋磁学中心特地主办 CM^2 Magazine，以期与各位地球科学工作者相互交流学习、合作共进！

“海洋孕育了生命，联通了世界，促进了发展”。 21 世纪是海洋科学的时代，由陆向海，让我们携手迈进中国海洋科学的黄金时代

目 录

岩石磁学演绎

第 20 章：磁相互作用对 ARM 的影响

根据尼尔理论得出的 ARM 表达式推断出只要很小的场，样品就能获得很大的 ARM 值，这显然与实验结果不符。为此，Jaep(1971)提出了磁相互作用对 ARM 的影响。

$$p_{ARM} = \tanh\left(\frac{M}{kT}(BH - \lambda p_{ARM})\right)$$

其中 $\lambda \approx M / r^3 \approx (4\pi / 3)M_s C$， $p_{ARM} = ARM / SIRM$ 。

由上式可知，当 ARM 逐渐增大时，由于引入的磁相互作用项-λp_{ARM}， 使得 ARM 不能无限增大，而是在场达到一定程度时达到饱和状态。磁相互作用力与两个颗粒之间的距离呈 $1/r^3$ 衰减。同时，磁相互作用里样品中的颗粒含量呈正比。因此，当样品中的磁性矿物含量增加时，磁性颗粒之间的磁相互作用力增加，从而使得样品 ARM 值减小。这比较合理地解释了实测数据。

磁相互作用对 ARM 影响很大。所以，如果不考虑磁相互作用，就很容易把 ARM 的变化简单地理解为 SD 颗粒的含量变化。之前我们学过 FORC 图是检测磁相互作用的好方法。

另外一种方法是比较 ARM 和 M_s，M_s 代表着磁性矿物总体含量的变化，如果 ARM 与 M_s 绝对正相关，这说明 ARM 确实受含量控制。如果 ARM/M_S 与 M_S 反相关，就说明随着磁性矿物含量的增加，ARM 相对变小，暗示着磁相互作用的影响不可忽略。

Li et al. (2012)系统地研究了磁相互作用对磁小体链获得 ARM 能力的影响。随着磁小体链的破碎与不断聚集，磁小体之间的相互作用逐渐加强。这主要体现在其 FORC 图在纵轴的展布逐渐加宽，样品获得 ARM 的能力逐渐降低。

在环境磁学研究中，ARM/SIRM 常被用做磁性颗粒的粒径参数，当 ARM/SIRM 增加时，一般暗示着磁性矿物颗粒的粒径减小。可是由图 1 可知，磁小体的粒径没有变，只是磁小体之间的相互作用力发生了变化，其 ARM/SIRM 的变化可以有一个数量级。

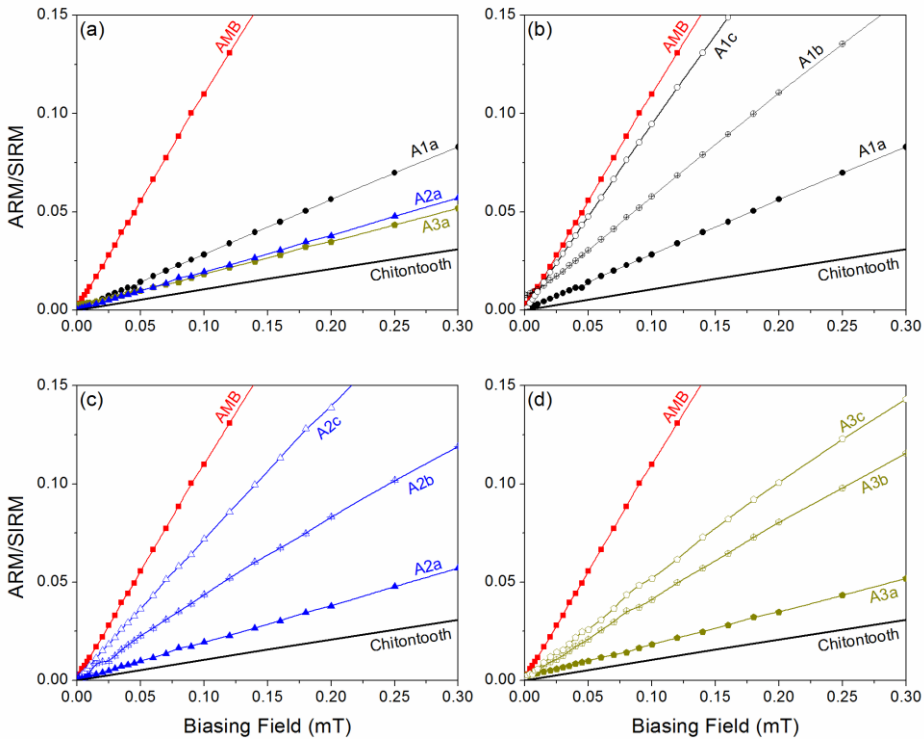

图 1 含有不同磁相互作用力磁小体链的样品 ARM/SIRM 随着 DC 外场增加的变化曲线。(Li et al., 2012)

Yamazaki et al. (1997)研究了太平洋中部沿着纬向分布(图 2a)样品的χ_{ARM}/χ_l (χ_l 为低频磁化率，以下简化为χ)。结果发现，该比值与样品的磁性矿物含量参数（比如磁化率和饱和等温剩磁）以及代表磁相互作用的参数 R 值具有明显的反

相关关系(图 2b)。因此，χ_{ARM}/χ并不能够简单地被用来代表磁性矿物粒径的变化。Yamazaki et al. (1997)认为 χ_{ARM}/χ与 log(χ)之间的线性趋势(图 2b)代表了磁相互作用对 ARM 的影响，χ_{ARM}/χ与该线性趋势之间的相对变化值$\Delta\chi_{ARM}/\chi$则可能消除这种影响。

通过对比$\Delta\chi_{ARM}/\chi$与χ_{ARM}/χ发现二者随纬度变化的趋势不完全一致。χ_{ARM}/χ在北纬 20 度左右出现峰值，个别点在北纬 50 度左右达到峰值。这些异常高点对应的样品磁性颗粒含量很低，因此χ_{ARM}/χ的异常高值应该与样品中弱磁相互作用有关。而$\Delta\chi_{ARM}/\chi$在南纬 10 度到北纬 20 度之间出现一个较为宽泛的稳定值，这代表着该区沉积物可能主要含有生物成因磁铁矿，而大气粉尘物质的输入较少。南纬 10 度左右的低值(粗颗粒)可能对应该区附近的火山喷山粉尘输入。综合$\Delta\chi_{ARM}/\chi$与χ_{ARM}/χ随纬度的变化模式，Yamazaki et al. (1997)认为前者的变化更为合理。

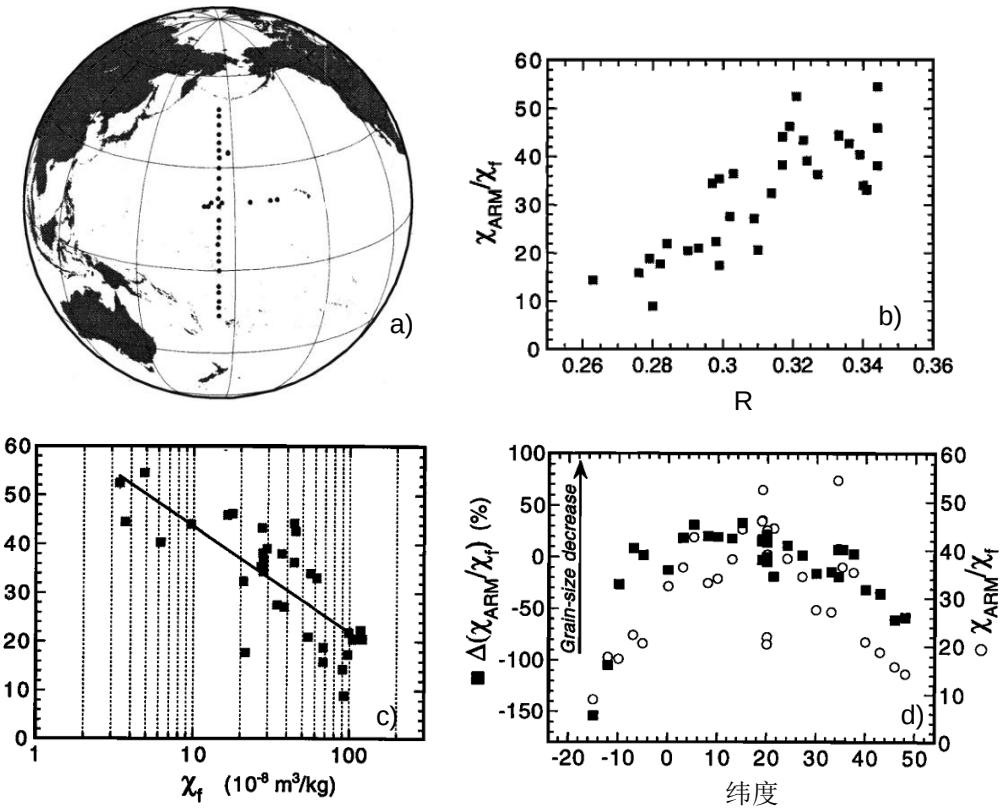

图 2 a) 样品采点；b) χ_{ARM}/χ_l 与磁相互作用参数 R 的相关图；b) χ_{ARM}/χ_l 与 χ_l 的相关图，横轴为对数坐标。直线代表由于磁相互作用造成的背景趋势。χ_{ARM}/χ_l 与背景趋势之间的相对偏差定义为$\Delta\chi_{ARM}/\chi_l$, 该参数被认为压抑了磁相互作用的影响; d) $\Delta\chi_{ARM}/\chi_l$(正方形)与χ_{ARM}/χ_l(空圈)随着纬度变化对比图。纵轴向上只是磁性颗粒粒径变细(改自 Yamazaki et al.，1997)。

上图 2c 的趋势只是一个经验关系，其合理性还需要更多的合成样品实验来证实，尤其对 SPD/MD 颗粒，磁相互作用对其携带 ARM 影响的研究还很欠缺。即使如此，Yamazaki et al.（1997）的研究方法值得借鉴。尤其当 ARM/SIRM 及 χ_{ARM}/χ与含量参数（更为合理的应该是 M_s）具有明显的反相关关系时，需要考虑磁相互作用是否影响了这些粒径参数。

胶黄铁矿在自然界中常常呈簇状聚集在一起，因此具有很强的磁相互作用，其 FORC 图在纵轴有很宽的展布。因此，当沉积序列中胶黄铁矿的信息比较显著时，不建议应用 ARM/SIRM 等粒径参数来指示粒径变化。

文献导读

1. 基于海洋自生钕同位素指标反演末次盛冰期以来全球翻转流演变

翻译人：仲义 zhongy@sustech.edu.cn

Jianghui Du, Brian A. Haley, Alan C. Mix, et al., ***Evolution of the Global Overturning Circulation since the Last Glacial Maximum based on marine authigenic neodymium isotopes*** *[J]. Quaternary Science Reviews, 2020, 241, 106396, 728-732.*

https://doi.org/10.1016/j.quascirev.2020.106396

摘要：全球翻转流与冰期-间冰期和千年时间尺度的气候变化密切相关。而对过去气候环流体系的理解仍然受到洋流替代指标之间的区别所阻碍。作者基于综合全球范围内末次盛冰期 Nd 同位素记录来重建洋流循环。我们提出从底到表解释出海水和自生 Nd 同位素不仅保存了海水混合信息，同时保存记录了受沉积影响的非保存行为。我们利用主成分分析提取自生 Nd 同位素的主要时空分布特征，并利用预算约束模型模拟的方法建立一阶环流模式。结果显示，在 LGM 时期，北大西洋翻转流的源区向南迁移，导致了更多放射性值更高冰期北边来源水（NSW）Nd 同位素输入。考虑到这种效应，我们推断冰期北大西洋具有和现今 NSW 的类似的组分，尽管冰期环流强度总体上呈现从北大西洋向南大洋来源减少的特征，但是增加了 Nd 同位素非保存行为的相对贡献量，并有可能促进更多碳被埋藏在深海中。在冰消期，我们发现南大洋翻转流开始增强，抵消北大西洋翻转流的减弱，并导致了全球深海环流的加强。更快的全球范围的冰消期环流会减少非保存效应的相对贡献，导致大西洋-太平洋深海 Nd 同位素的汇聚。南大洋翻转流的转变可能会驱动冰消期大气 CO2 和全球热量平衡的变化。

ABSTRACT: The Global Overturning Circulation is linked to climate change on glacial-interglacial and multimillennial timescales. The understanding of past climate-circulation links remains hindered by apparent conflicts among proxy measures of circulation. Here we reconstruct circulation changes since the Last Glacial Maximum (LGM) based on a global synthesis of authigenic neodymium isotope records (εNd). We propose the bottom-up framework of interpreting seawater and authigenic εNd considering not only conservative watermass mixing, but also the preformed properties and the non-conservative behavior of εNd, both subject to sedimentary

influences. We extract the major spatial-temporal modes of authigenic εNd using Principal Component Analysis, and make a first-order circulation reconstruction with budget-constrained box model simulations. We show that during the LGM, the source region of North Atlantic overturning shifted southward, which led to more radiogenic preformed εNd of glacial Northern Source Water (NSW). Considering this preformed effect, we infer that glacial deep Atlantic had a similar proportion of NSW as today, although the overall strength of glacial circulation appears reduced from both North Atlantic and Southern Ocean sources, which increased the relative importance of nonconservative behavior of εNd and may have facilitated accumulation of respired carbon in the deep ocean. During the deglaciation, we find that Southern Ocean overturning increased, which offset suppressed North Atlantic overturning and resulted in a net stronger global abyssal circulation. Faster global scale deglacial circulation reduced the relative importance of non-conservative effects, resulting in AtlanticPacific convergence of abyssal εNd signatures. Variations of Southern Ocean overturning likely drove a significant fraction of deglacial changes in atmospheric CO2 and oceanic heat budget.

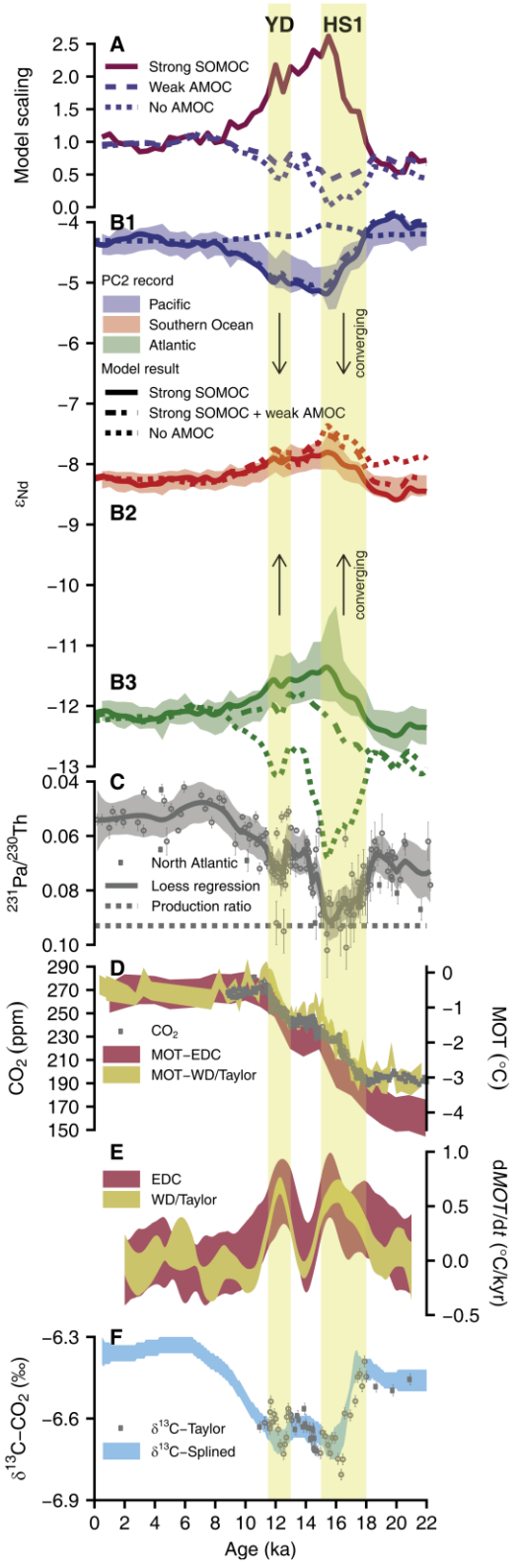

Figure 1. Observed and simulated deglacial authigenic εNd records compared to global climate proxies. A: Model scaling (with respect to the Holocene mean) applied to the SOMOC (scaled to median PC2 scores in Fig. 5B) and the AMOC (scaled to North Atlantic 231Pa/230Th LOESS regression median in C) in simulations. B: Model results (lines, labels corresponding to the scaling in A) compared to the PC2 records (ribbons) of representative high resolution authigenic εNd

records from North Pacific (B1, EW0408-87JC, 3680 m) (Du et al., 2018), Southern Ocean (B2, PS75/073_2, 3234 m) (Basak et al., 2018) and North Atlantic (B3, OCE326_GGC6/ODP Site1063, 4543 m)(Bohm et al., 2015 € ; Lippold et al., 2019; Roberts et al., 2010). The mean εNd offset between each individual site and the ocean box average is removed to facilitate datamodel comparison. C: 231Pa/230Th records from the North Atlantic (Ng et al., 2018) (dots for raw data; solid line and ribbon for LOESS regression median and 95% CI). 0.093 (dotted line) is the production ratio. D: Ice Core CO2 from WAIS Divide (WD) (Marcott et al., 2014) and noble gas derived Mean Ocean Temperature (MOT) anomaly from EPICA Dome C (EDC) and WD. The YD interval of WD record is replaced by Taylor Glacier data (Baggenstos et al., 2019; Bereiter et al., 2018; Shackleton et al., 2019). E:Rate change of MOT (dMOT/dt) estimated using nonparametric kernel regression smoothing with a global bandwidth of 1.5 kyr. F: Ice core d13C-CO2 from Taylor Glacier (Bauska et al., 2016) and a spline-smoothed compilation (Schmitt et al., 2012).

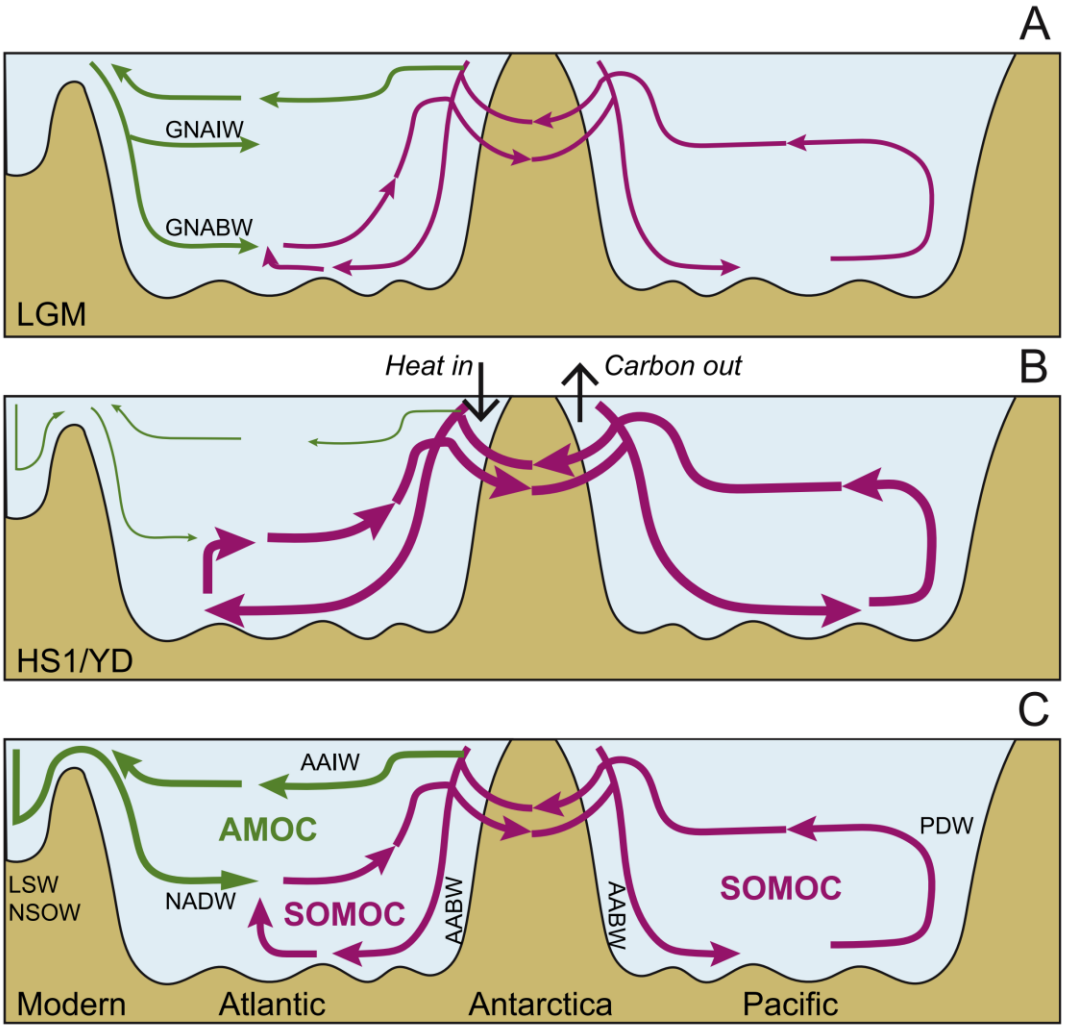

Figure 2. Schematics of ocean circulation in the LGM (A), HS1 and YD (B), and today (C). The modern scheme is based on Talley (2013). Note inferred Glacial North Atlantic Intermediate and Bottom Water (GNAIW and GNABW). For schematics LSW and NSOW appear together but separated from the North Atlantic basin. The thickness of the lines indicates hypothetical transport strength. For εNd-based NPIW reconstruction we refer to our previous study (Du et al., 2018) where we found it to not have changed significantly since the LGM.

2. 现今浮游植物浓度变化驱动北冰洋初级生产力增强

翻译人：蒋晓东 jiangxd@sustech.edu.cn

Lewis, K. M., van Dijken, G. L., Arrigo K. R. (2020). ***Changes in phytoplankton concentration now drive increased Arctic Ocean primary production****. Science. 369, 198-202.*

摘要：历史上北冰洋海冰消退被认为促进初级生产力增加，因为海冰消退使大洋海水进入并且出现长时间的生长季节。然而关于初级生产力持续增加是否海冰应该进一步消退的问题一直存在争议。本研究使用海洋颜色算法使北冰洋相关信息数字化，发现在 1998 年到 2018 年间初级生产力增加了 57%。前十年的增加是因为广泛的海冰消退，而后十年主要由增强的浮游植物量引起。浮游植物两的持续增强很可能由新的营养盐输入引起。这意味着未来北冰洋可支持更高营养级产力和额外的碳输出。

ABSTRACT： Historically, sea ice loss in the Arctic Ocean has promoted increased phytoplankton primary production because of the greater open water area and a longer growing season. However, debate remains about whether primary production will continue to rise should sea ice decline further. Using an ocean color algorithm parameterized for the Arctic Ocean, we show that primary production increased by 57% between 1998 and 2018. Surprisingly, whereas increases were due to widespread sea ice loss during the first decade, the subsequent rise in primary production was driven primarily by increased phytoplankton biomass, which was likely sustained by an influx of new nutrients. This suggests a future Arctic Ocean that can support higher trophic-level production and additional carbon export.

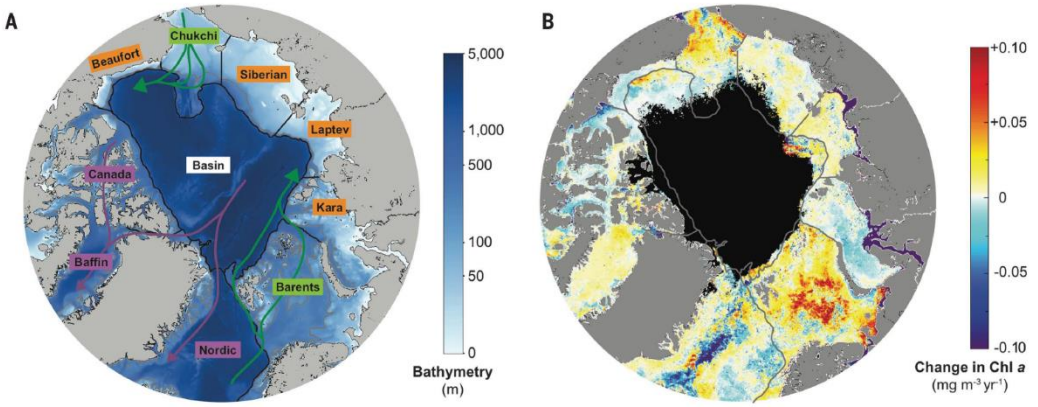

Fig 1: Regions of interest and changes in phytoplankton biomass. (A) The AO with its shelf seas and basin. Subregions are bounded by black lines by using the 1000-m isobath and categorized as inflow

(green), interior (orange), or outflow (purple) shelves. The 200-m isobath is shown in gray. Inflow and outflow currents are depicted as green and purple arrows, respectively. (B) The rate of change in Chl a (milligrams per cubic meter per year) between 1998 and 2018. Subregions are delineated by gray lines. Black pixels indicate no data.

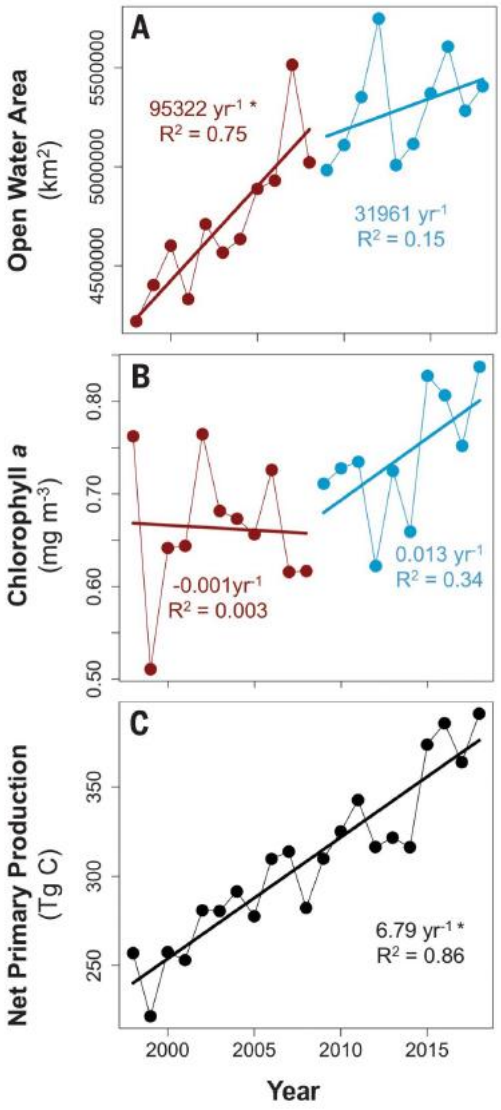

Fig 2: AO time series trends. (A to C) Annual time series of AO (A) mean OW area, (B) mean Chl a, and (C) NPP. Results from regression analysis for the entire (1998–2018), early (1998–2008), and recent (2009–2018) parts of the time series are in black, red, and blue, respectively, with significant trends ($P < 0.05$) indicated by an asterisk.

3. 不同的深部地幔域形成历史反映在地球化学的差异上

翻译人：冯婉仪 fengwy@sustech.edu.cn

Doucet L S, Li Z X, El Dien H G, et al. ***Distinct formation history for deep-mantle domains reflected in geochemical differences****[J].* ***Nature geoscience****, 2020, 13: 511-515.*

摘要：目前地球的地幔被环太平洋俯冲带划分为非洲和太平洋两个地幔域，并且每个地幔域中的下地幔都以一个大的低剪切波速区（LLSVP）为特征。然而，对于 LLSVPs 在时间上是静止的还是随着全球俯冲几何结构的变化而变化的，仍然存在争议。在这里，我们整理了来自这两个 LLSVPs 之上的洋岛和海洋高原的地幔柱成因玄武岩的放射性同位素数据，这些数据显示这两个地幔域中具有显著不同的铅、钕和锶同位素组成。在 Pangaea 超大陆的形成和裂解过程中，非洲地幔域受到了俯冲大陆物质的富集作用，而太平洋地幔域没有发现这种特征。这种深部地幔地球化学的差异反映了两个地幔域在 Rodinia 和 Pangaea 超大陆旋回期间的不同演化历史，因此，这支持了板块构造和深部地幔结构的动态关系。

ABSTRACT: The Earth’s mantle is currently divided into the African and Pacific domains, separated by the circum-Pacific subduction girdle, and each domain features a large low shear-wave velocity province (LLSVP) in the lower mantle. However, it remains controversial as to whether the LLSVPs have been stationary through time or dynamic, changing in response to changes in global subduction geometry. Here we compile radiogenic isotope data on plume-induced basalts from ocean islands and oceanic plateaus above the two LLSVPs that show distinct lead, neodymium and strontium isotopic compositions for the two mantle domains. The African domain shows enrichment by subducted continental material during the assembly and breakup of the supercontinent Pangaea, whereas no such feature is found in the Pacific domain. This deep-mantle geochemical dichotomy reflects the different evolutionary histories of the two domains during the Rodinia and Pangaea supercontinent cycles and thus supports a dynamic relationship between plate tectonics and deep-mantle structures.

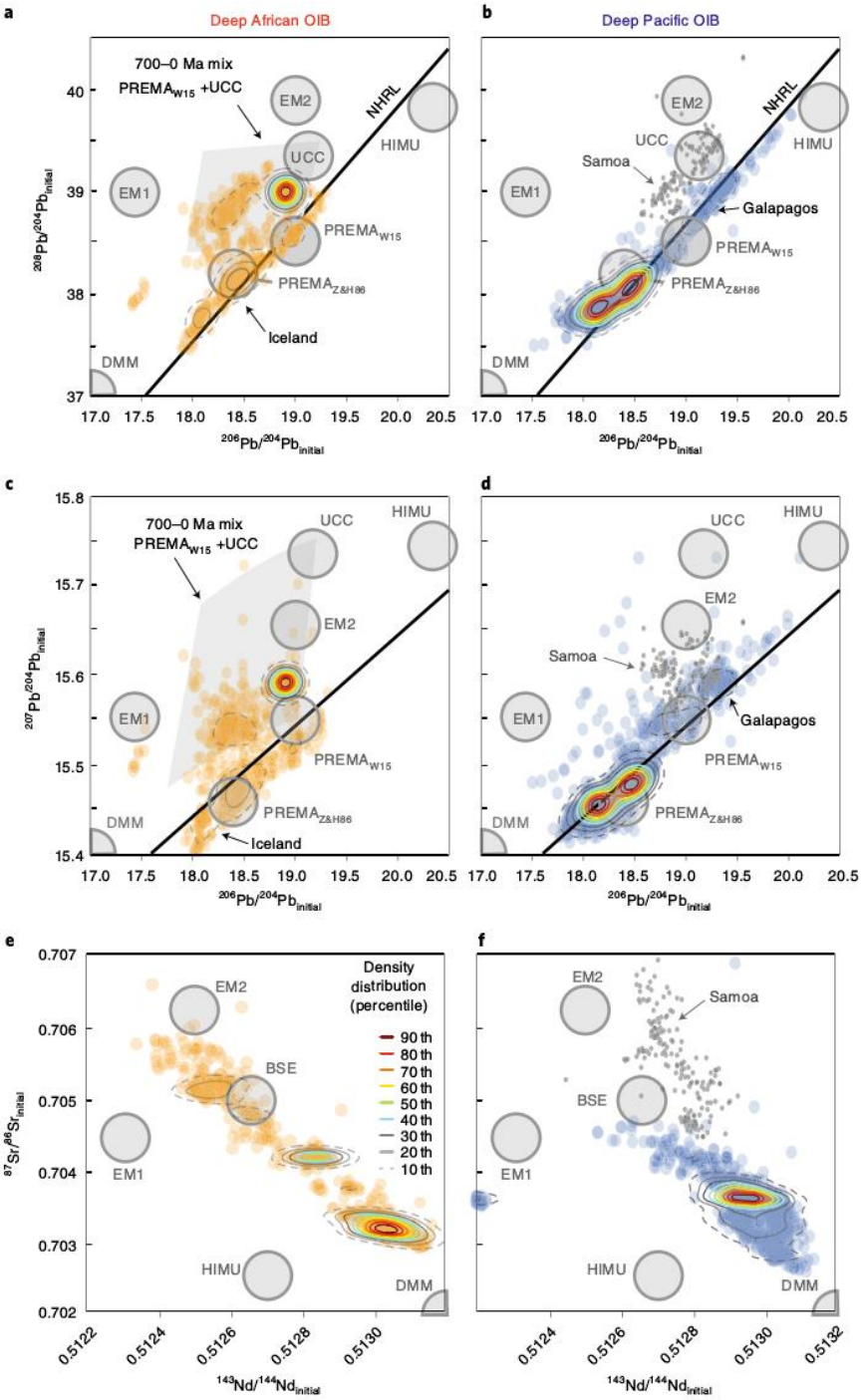

Figure 1. Isotopic data of OIBs and OPBs derived from the deep source of the African and the Pacific mantle domains. Isotopic compositions are back-calculated to initial compositions at the time of crystallization for Kerguelen and Ontong Java oceanic plateaus. a,b, $^{206}Pb/^{204}Pb$ versus $^{208}Pb/^{204}Pb$. c,d, $^{206}Pb/^{204}Pb$ versus $^{207}Pb/^{204}Pb$. e,f, $^{143}Nd/^{144}Nd$ versus $^{87}Sr/^{86}Sr$. The contour lines represent percentiles of the kernel density estimation (see Methods). Also shown are the NHRL[16] that defines the DUPAL anomaly (above the NRHL), the prevalent mantle defined by Zindler and Hart[38] ($PREMA_{Z\&H86}$) and by White[13] ($PREMA_{W15}$), enriched mantle 1 (EM1), enriched mantle 2 (EM2), high-μ (HIMU) and the UCC isotopic endmembers[13]. The grey fields shown in a and c are mixing modelling results of $PREMA_{W15}$+ UCC between 700 and 0 Ma.

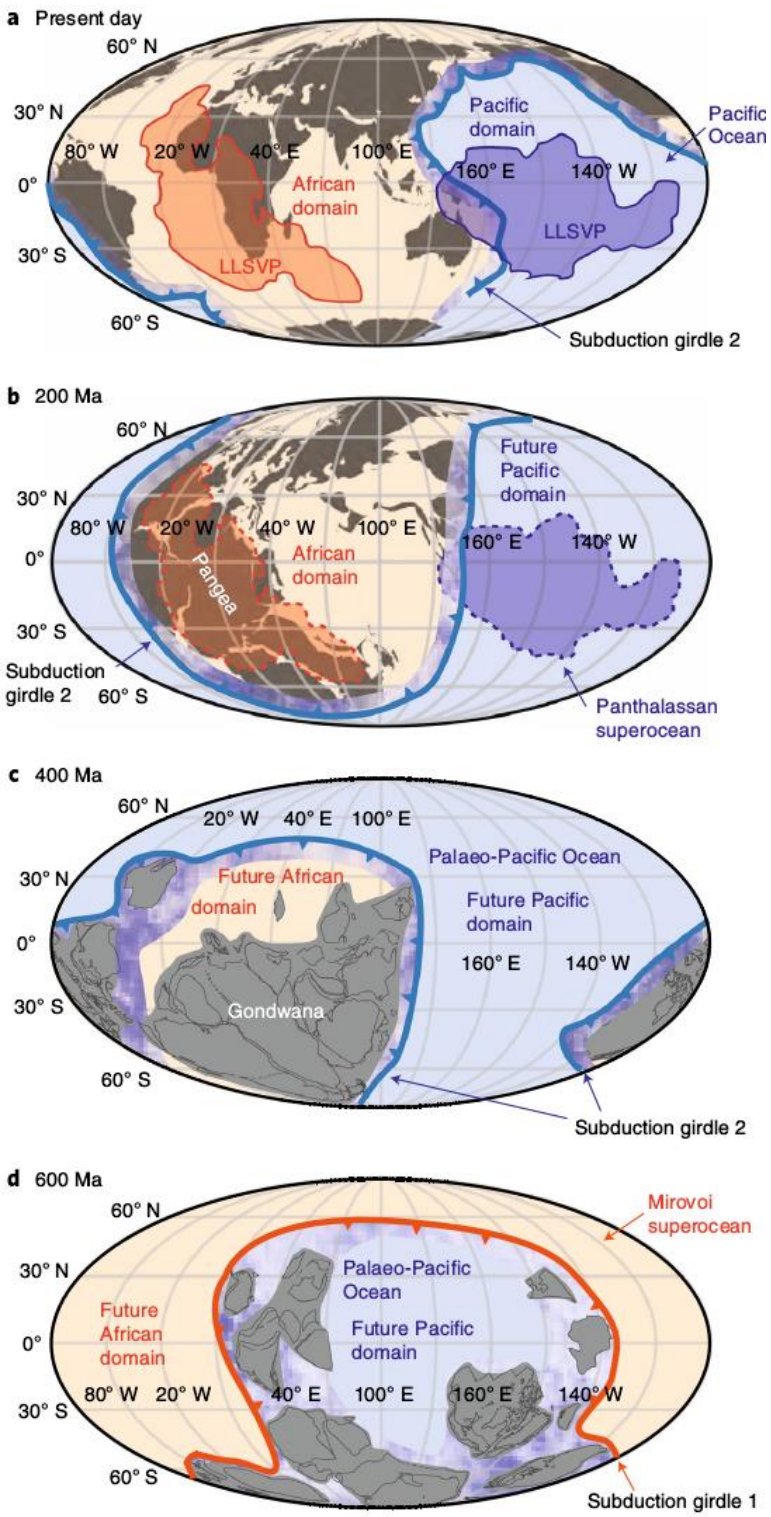

Figure 2. Configurations of the continental masses and African and Pacific mantle domains for the present day, 200 Ma, 400 Ma and 600 Ma. a, Present-day configuration with positions of the two mantle domains and their respective LLSVPs (orange for the African domain and blue for the Pacific domain) and the circum-Pacific subduction girdle. b, Pangaea configuration at 200 Ma[39]. c, Pangaea assembly process at 400 Ma[35]. d, Rodinia break-up and Gondwana assembly at 600 Ma[35]. Note the contour shapes of the LLSVPs in b are speculative and based on their present-day configuration. The maps are centred on the Equator and 100th meridian, and each meridian is separated by 30°.

4. 在 Thellier 式实验中非理想样品的热和微波退磁方法估计值的比较

翻译人:李园洁 liyj3@sustech.edu.cn

Grappone, J. M., Biggin, A. J., Barrett, T. J., Hill, M. J., & Sprain, C. J. ***Comparison of thermal and microwave paleointensity estimates in specimens displaying non -ideal behavior in Thellier - style paleointensity experiments****[J]. Journal of Geophysical Research: Solid Earth, 2020, 125. doi:10.1029/2020JB019802*

摘要：确定地磁场古强度的变化对我们理解地核和地球发电机过程具有重要意义，但是获得可靠的古强度值仍存在困难。全球古强度数据库中 0-5 Ma 的地磁场强度观测值有超过四分之一来自夏威夷。前人在 SOH1 钻孔的两项研究用不同的方法估计古强度，给出不一样的结果，相差 30%。这两项研究中采用的古强度方法的退磁机制（热或微波辐射）和 Thellier 式检验方法均不同是导致结果巨大差异的原因。因此本文利用之前未试过的热-垂直和微波-原始 Thellier 方法的综合来对 79 个样品进行古强度实验，来分析退磁机制和退磁方法单独的影响。我们发现退磁机制还是退磁方法都不能完全解释古强度结果的差异。另外，我们发现利用原始 Thellier 退磁方法时非理想多畴效应会增强，导致估计的古强度过高。微波-垂直实验没有 pTRM 检验会产生过低的古强度，这是由于未计算较高微波能量下样品蚀变，这支持了最近 1960 Kilauea 熔岩的发现。这些发现也证明真实的古强度介于前人结果之内，需要 pTRM 检验和探测非理想颗粒效应的方法做进一步的研究（热或微波）。

ABSTRACT： Determining the strength of the ancient geomagnetic field is vital to our understanding of the core and geodynamo but obtaining reliable measurements of the paleointensity is fraught with difficulties. Over a quarter of magnetic field strength estimates within the global paleointensity database from 0-5 Ma come from Hawai‘i. Two previous studies on the SOH1 drill core gave inconsistent, apparently method-dependent paleointensity estimates, with an average difference of 30%. The paleointensity methods employed in the two studies differed both in demagnetization mechanism (thermal or microwave radiation) and Thellier-style protocol (perpendicular and Original Thellier protocols) - both variables that could cause the strong differences in the estimates obtained. Paleointensity experiments have therefore been conducted on 79 specimens using the previously untested combinations of Thermal-Perpendicular and Microwave-Original Thellier methods to analyze the effects of demagnetization mechanism and protocol in isolation. We find that, individually, neither demagnetization mechanism nor protocol

entirely explains the differences in paleointensity estimates. Specifically, we found that non-ideal multi-domain-like effects are enhanced using the Original Thellier protocol (independent of demagnetization mechanism), often resulting in paleointensity overestimation. However, we also find evidence, supporting recent findings from the 1960 Kilauea lava flow, that Microwave-Perpendicular experiments performed without pTRM checks can produce underestimates of the paleointensity due to unaccounted-for sample alteration at higher microwave powers. Together, these findings support that the true paleointensities fall between the estimates previously published and emphasize the need for future studies (thermal or microwave) to use protocols with both pTRM checks and a means of detecting non-ideal grain effects.

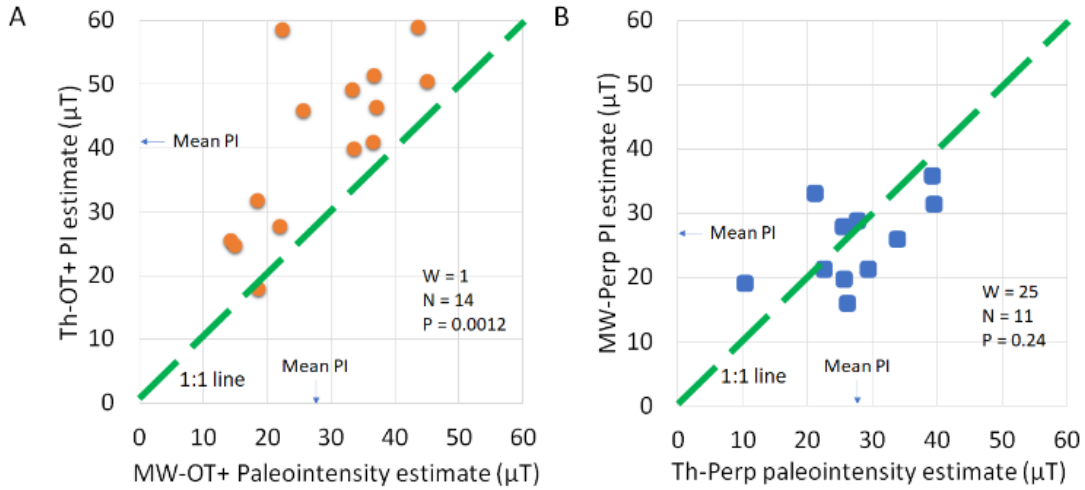

Figure 1. Testing the hypothesis that only demagnetization mechanism matters. Flow-level paleointensity estimates are plotted against each other for different PI methods, separated by protocol.A: Original Thellier data; B: perpendicular data. The mean PIs listed are for the flows the methods have in common. N is the number of data points, W and p are the statistics from the Wilcoxon signed rank test.

5. 地球观测和数值模拟揭示的地磁场快速变化

翻译人：柳加波

Davies, C.J., Constable, C.G., 2020. ***Rapid geomagnetic changes inferred from Earth observations and numerical simulations.*** *Nat. Commun. 11, 3371.*

http://dx.doi.org/10.1038/s41467-020-16888-0

摘要：极端地磁场方向变化包含了地球发电机模型运作的重要信息。古地磁研究已经报道了 1° yr^{-1} 的快速地磁场方向变化。但是这些古地磁结果仍存在争议，并且我们对方向快速变化和地球内核物理过程之间的关系仍缺乏了解。本文我们展示了一系列的地球发电机模拟和过去 100kyrs 地磁场观测模型在极端方向变化的幅度和纬度上存在极好的一致性。尤其是在地磁场强度下降的时间段，最大的方向变化速率达到了~10° yr^{-1}，几乎是现今地磁场变化速率的 100 倍。对模拟和一个简单的模拟模型的详细分析显示，极端的方向变化和地核表面的反向通量移动有关。我们的结果证实快速的方向变化是和地球发电机模型的物理机制相兼容的。并且，未来对快速地磁场方向变化的研究应该更关注低纬度地区。

ABSTRACT： Extreme variations in the direction of Earth's magnetic field contain important information regarding the operation of the geodynamo. Paleomagnetic studies have reported rapid directional changes reaching 1° yr^{-1}, although the observations are controversial and their relation to physical processes in Earth's core unknown. Here we show excellent agreement between amplitudes and latitude ranges of extreme directional changes in a suite of geodynamo simulations and a recent observational field model spanning the past 100 kyrs. Remarkably, maximum rates of directional change reach ~10° yr^{-1}, typically during times of decreasing field strength, almost 100 times faster than current changes. Detailed analysis of the simulations and a simple analogue model indicate that extreme directional changes are associated with movement of reversed flux across the core surface. Our results demonstrate that such rapid variations are compatible with the physics of the dynamo process and suggest that future searches for rapid directional changes should focus on low latitudes.

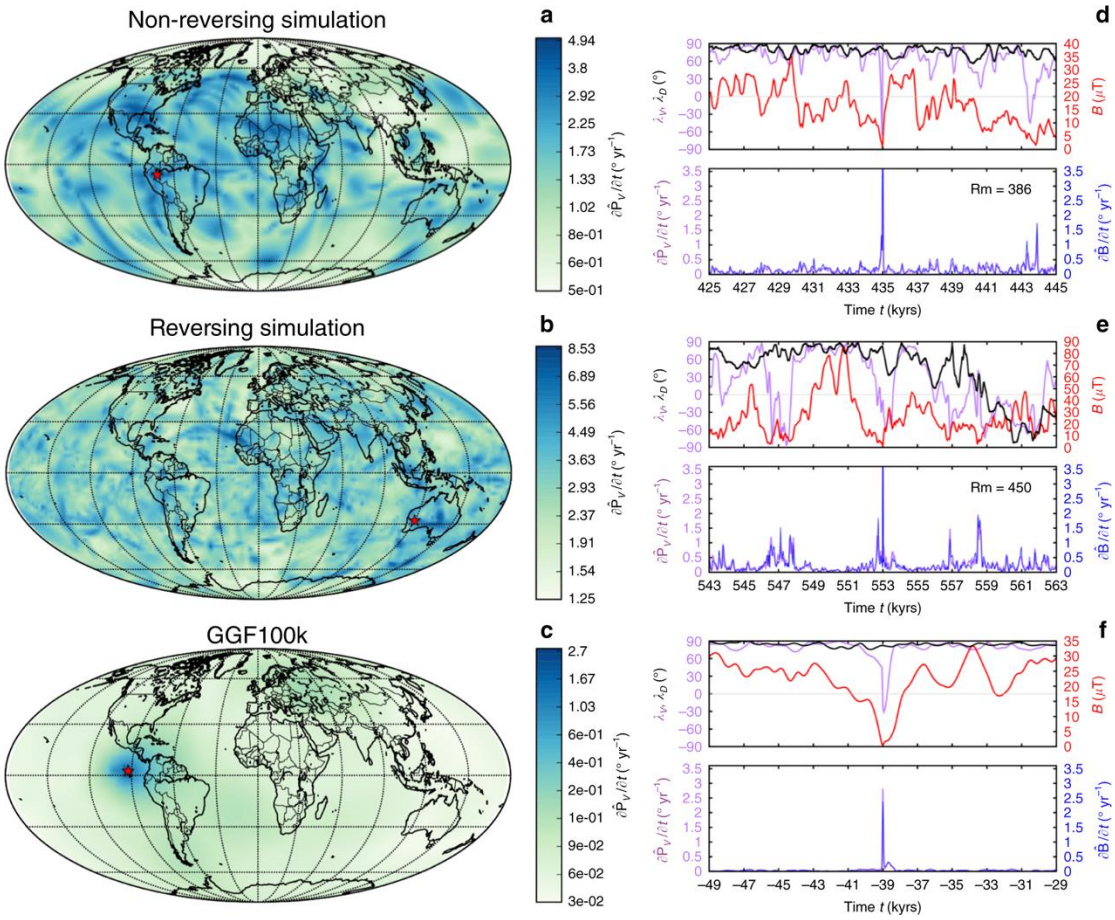

Fig 1: Rapid directional changes in two geodynamo simulations and GGF100k. Shown are a non-reversing simulation with magnetic Reynolds number $Rm = 386$ (**a**, **d**), a reversing simulation with $Rm = 450$ (**b**, **e**) and the observational field model GGF100k (**c**, **f**). Left column shows Mollweide projections at Earth's surface of the largest change in VGP position, $\partial\widehat{\boldsymbol{P}}_V/\partial t$, as a function of location in °yr^{-1}. Red stars show the location of $(\partial\widehat{\boldsymbol{P}}_V/\partial t)_{ex}$ on each plot. Note the different colour scales and that values at each location may not have occurred at the same point in time. Right-hand panels show directional data at the locations of $(\partial\widehat{\boldsymbol{P}}_V/\partial t)_{ex}$ over a 20 kyr period with the extreme event at the midpoint. Here the top row of each panel shows the latitude λ_V of $\partial\widehat{\boldsymbol{P}}_V$ (purple), the dipole latitude λ_D (black), and the field strength B (red); the bottom row shows $\partial\widehat{\boldsymbol{P}}_V/\partial t$ (purple) and the rate of change of the field vector $\partial\widehat{\boldsymbol{B}}_V/\partial t$ (blue). Simulations have been run for 232 kyrs for $Rm = 386$ and 415 yrs for $Rm = 450$.

6. 菲律宾海板块俯冲的年龄与低频地震发生机制

翻译人：刘伟 inewway@163.com

Hua Y, Zhao D, Xu Y, et al. ***Age of the Subducting Philippine Sea Slab and Mechanism of Low-Frequency Earthquakes****[J].* ***Geophysical Research Letters****, 2018, 45(5): 2303-2310.*

摘要：非火山低频地震（LFEs）是近年来广泛观测到的地震，通常发生在环太平洋地区的年轻温暖的俯冲带，有时可能成为大强度地震的前兆。然而，LFEs 的生成机制尚不十分清楚。本文估计了菲律宾海板块俯冲时岩石圈的年龄，发现岩石圈年龄与日本西南部 LFE 分布密切相关。在 Kii channel 上存在 LFE 间断。我们认为，这一间断是由多个因素的共同作用造成的，包括最年轻的板块年龄、高温、流体含量低、上覆板块的高渗透率、板块撕裂和菲律宾海板块下方的上涌热流。研究结果对 LFEs 的形成机理和俯冲动力学有了新的认识。

ABSTRACT: Nonvolcanic low-frequency earthquakes (LFEs) have been widely observed in recent years, which usually occur in young and warm subduction zones in the circum-Pacific regions and sometimes may become precursors of large megathrust earthquakes. However, the generating mechanism of the LFEs is still not very clear. In this study we estimate the lithosphere age of the subducting Philippine Sea slab and find a close relationship between the slab age and the LFE distribution in SW Japan. An LFE gap exists at the Kii channel. We think that the gap is caused by joint effects of several factors, including the youngest slab age, high temperature, low fluid content, high permeability of the overlying plate, a slab tear, and hot upwelling flow below the Philippine Sea slab. The present results shed new light on the generating mechanism of the LFEs and subduction dynamics.

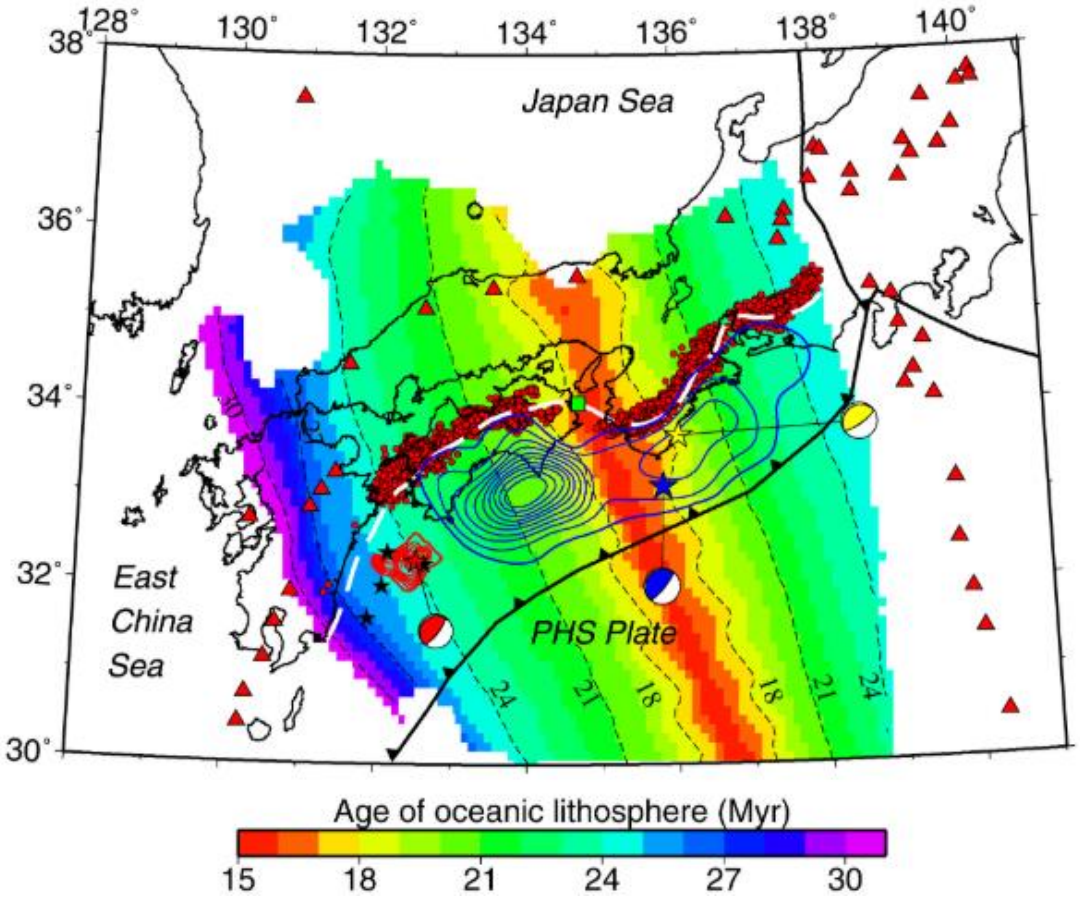

Figure 1. The colors show the estimated oceanic lithosphere ages of the subducting Philippine Sea (PHS) slab, whose scale is shown at the bottom. The white dashed line denotes the 30 km depth contour of the upper boundary of the PHS slab. The red dots denote nonvolcanic low-frequency earthquakes recorded by the seismic network (Hi-net) during 2002 to 2016 (Japan Meteorological Agency: http://www.jma.go.jp). The thin black dashed lines show the contours of the lithosphere age. The black lines show the plate boundaries. The red triangles denote active volcanoes. The blue contour lines denote the coseismic slip areas of the 1944 M w 8.1 Tonankai (yellow star) and the 1946 M w 8.3 Nankai (blue star) megathrust earthquakes (Sagiya & Thatcher, 1999). The red contour lines denote the coseismic slip area of the 1968 M w 7.5 Hyuganada megathrust earthquake (red star) (Yagi et al., 1998). The beach balls with different colors show focal mechanism solutions of the three large megathrust earthquakes determined by Kanamori (1972) and Yagi et al. (1998). The black stars denote epicenters of megathrust earthquakes (M > 7.0) that occurred during 1900 to 2013.

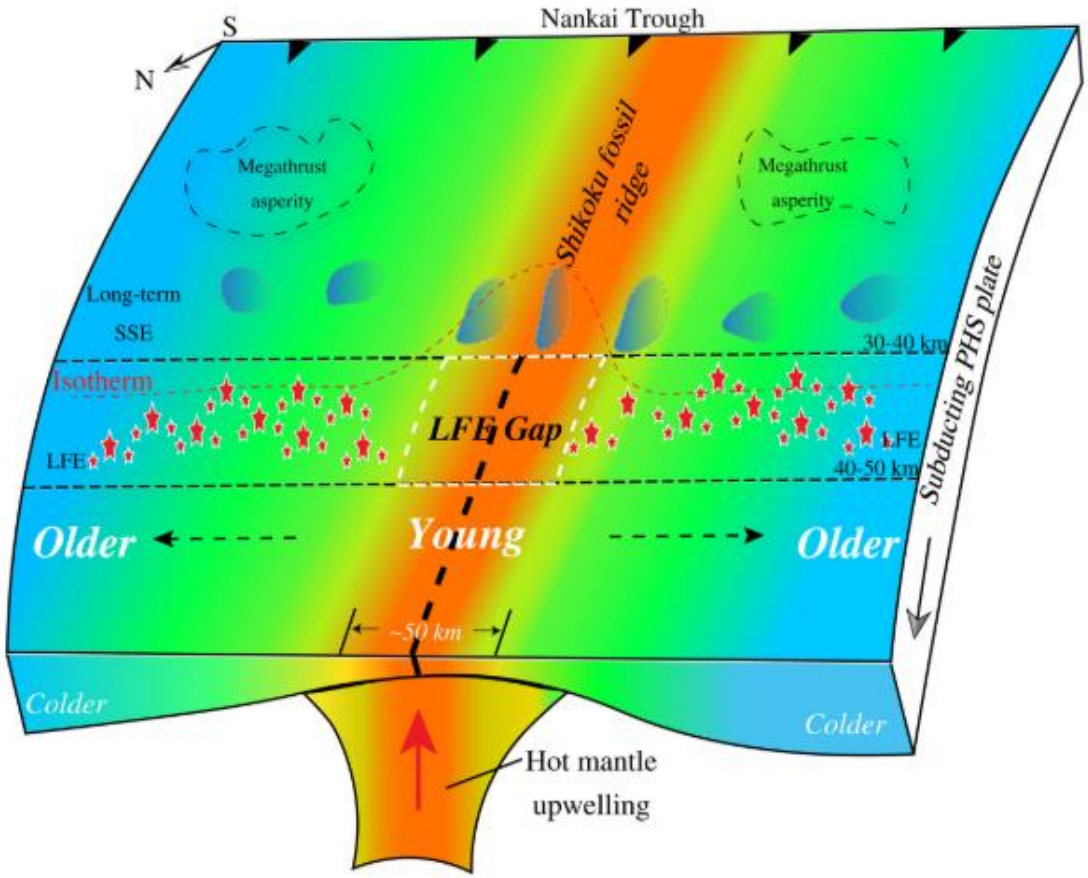

Figure 2. A schematic model showing the cause of the LFE (low-frequency microearthquake) gap. The red stars denote the LFEs. The thick black dashed line denotes a possible slab tear associated with the fossil Shikoku spreading ridge. See the text for details.

7. 通过蒙赛尔图表与漫反射光谱测定巴西亚热带土壤颜色

翻译人：曹伟

Ramos P V , Inda A V , Vidal Barrón, et al. ***Color in subtropical brazilian soils as determined with a Munsell chart and by diffuse reflectance spectroscopy****[J].* ***CATENA****, 2020, 193:104609.*

摘要：土壤的颜色提供了反映其来源的有用信息，并能以此进行分类。传统方法常使用蒙赛尔图表法确定土壤颜色，而目前例如漫反射光谱（DRS）这样的替代技术使定量变得更加精确。在本项研究中，我们对蒙赛尔图标法和漫反射光谱法所测定的色调、色度、红度等颜色参数进行比较。通过 DRS 测量获得的数据被用于绘制巴西南里奥格兰德州（RS）的精确土壤颜色图。同时，通过 DRS 数据可以动态连续计算巴西土壤的[赤铁矿/（赤铁矿+针铁矿）][Hm/(Hm+Gt)]。根据这些比值，可以将土壤划分为针铁矿型[Hm/(Hm+Gt) ≤25%]，针铁矿-赤铁矿型[25<Hm/(Hm+Gt)≤50%]，赤铁矿-针铁矿型[50<Hm/(Hm+Gt)≤75%]以及赤铁矿型[Hm/(Hm+Gt)≥25%]。两种方法测得的颜色参数存在差异，通过蒙赛尔图表法往往高估或低估 DRS 测量结果。基于[Hm/(Hm+Gt)]比值，所描述的目标土壤主要是针铁矿型。

ABSTRACT：The color of soils provides useful information about their origin and allows their classification. Soil color has traditionally been determined with a Munsell chart; lately, however, alternative techniques such as diffuse reflectance spectroscopy (DRS) have enabled more accurate quantification. In this work, we determined the color parameters hue, value, chroma and reddening index using a Munsell chart and a DRS instrument for comparison. The data obtained from the DRS measurements were used to develop an accurate soil color map for the Rio Grande do Sul state in Brazil (RS). DRS data were also used for removable continuum calculations to determine the [hematite/(hematite + goethite)] ratio [Hm/(Hm + Gt)] of Brazilian soils. Based on suchratio, the soils were classified as goethitic [Hm/(Hm + Gt) ≤ 25%], goethitic–hematitic [25 < Hm/(Hm + Gt) ≤ 50%], hematitic–goethitic [50 < Hm/(Hm + Gt) ≤ 75%] or hematitic [Hm/(Hm + Gt) ≥ 25%]. Color parameters differed between the two measurement methods, with the Munsell chart often overestimating or underestimating the DRS results. Based on the [Hm/(Hm + Gt)] ratio, the target soils were mainly goethitic.

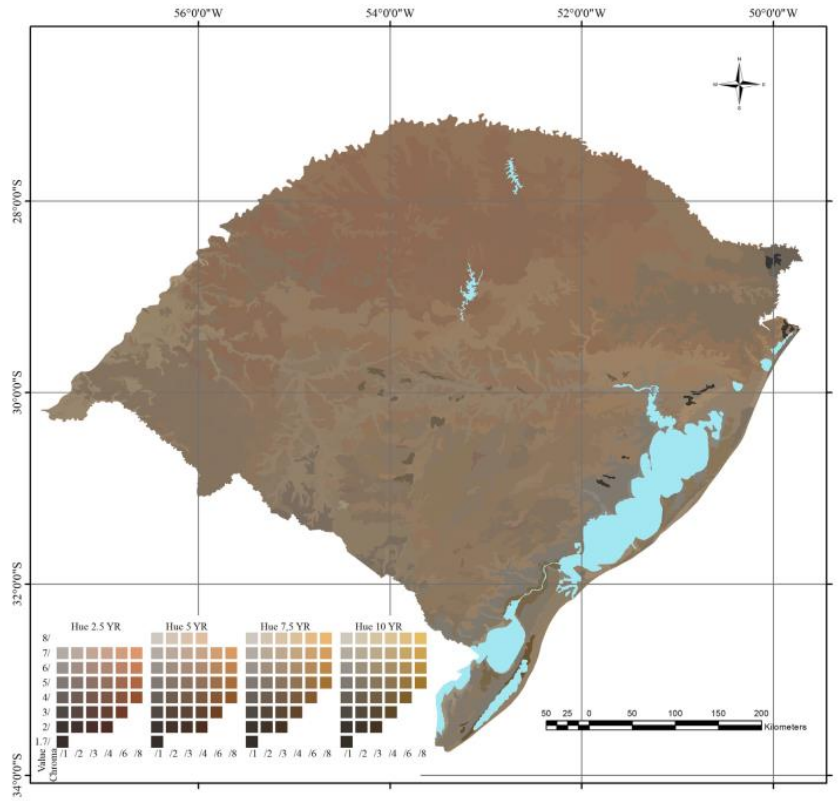

Fig. 1 Surface color of the soils as determined by DRS

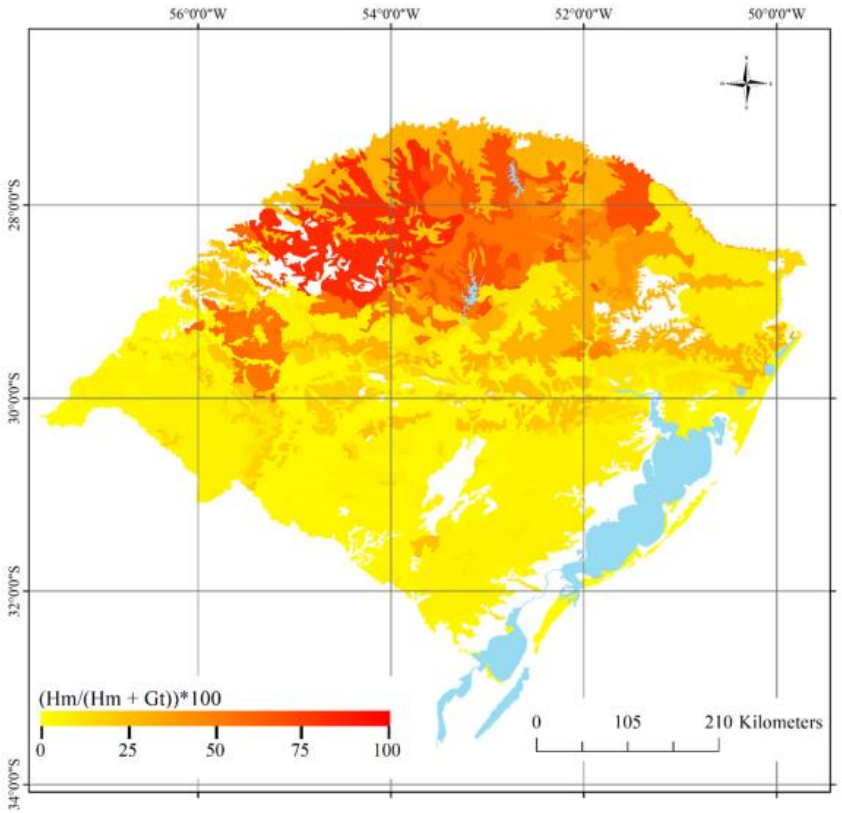

Fig. 2 Hm/(Hm + Gt) ratio for the soils as determined from DRS data. No ratio was assigned to the white polygons.

8. 北 California 的多指标石笋记录揭示区域水汽在末次冰期的动态模式

翻译人：杨会会 11849590@mail.sustech.edu.cn

Oster G L, Weisman I E, Sharp W D et al. ***Multi-proxy stalagmite records from northern California reveal dynamic patterns of regional hydroclimate over the last glacial cycle[J].Quaternary science reviews,****2020,241,106411*

https://doi.org/10.1016/j.quascirev.2020.106411

摘要：尽管降雨对加利福尼亚州的水资源很重要，但人们对北加州的降水量在器测时期以前是如何变化的知之甚少。本文呈现了一个新的来自加利福尼亚州沙斯塔湖岩洞(LSC)，两根同期石笋的多指标古气候记录，该记录涵盖了从 MIS 3 到 H1 时段(~35,000 - 14,000 years BP)。LSC 位于美国西北部和西南部地区之间的过渡地带，这个地区显示出降水对现代和古气候驱动因素的不同响应。LSC 石笋的稳定同位素和微量元素指标表明，该地区在 D-O 旋回有关的冰期间(暖期)为湿润气候条件，类似于俄勒冈南部和北部大盆地的记录，但与西南沙漠的记录相反。与北部的喀斯卡德山脉和落基山脉相似，LSC 在末次冰期更加干燥。然而，多种指标表明在 H1 期间降雨增加，这与大盆地和西南部地区类似。因此，LSC 的记录证明了过渡带位置的不稳定性，并说明了美国西部降水对全球气候变化的反应的复杂模式。降雨指标 $\delta^{18}O$ 与 $\delta^{13}C$ 和微量元素的协同变化，表明末次间冰期，尽管本地气候更加干燥，但来自中部太平洋的降雨比例更高；相反，以降水量增加为特征的时期，如 H1 早期，本地降雨增加则与来自北太平洋的水汽增强有关。

ABSTRACT: Despite its importance for California's water resources, little is known about how precipitation has varied in far northern California beyond the historical record. We present a new, multi-proxy paleoclimate record derived from two coeval stalagmites from Lake Shasta Caverns (LSC), California that covers the end of Marine Isotope Stage 3 through Heinrich Stadial 1 (~35,000 to 14,000 years BP). At 40.8N, LSC is situated within the transition zone between regions in the northwestern and southwestern United States that demonstrate different precipitation responses to both modern and paleoclimatic drivers. Stable isotope and trace element proxies from LSC stalagmites indicate the region experienced wet conditions during interstadials (warm periods) associated with Dansgaard-Oeschger cycles, similar to proxy records from southern Oregon and the northern Great Basin, but in contrast to records from the desert southwest. Similar to the northern Cascades and Rocky Mountains, LSC was drier during the Last Glacial Maximum. However, proxies indicate increased rainfall throughout Heinrich Stadial 1, similar to the Great Basin and southwest. Thus, the LSC record demonstrates the non-stationarity of the transition zone location and illustrates a complex pattern of precipitation response to global climate change in the western United States. Covariation of speleothem $\delta^{18}O$, an indicator of moisture source, with $\delta^{13}C$ and trace

elements, indicators of moisture amount, suggest a higher proportion of Central Pacific precipitation during the Last Glacial Maximum, despite the enhanced aridity. In contrast, periods characterized by increased precipitation amounts, such as early Heinrich 1, are associated with enhanced moisture from the Northern Pacific.

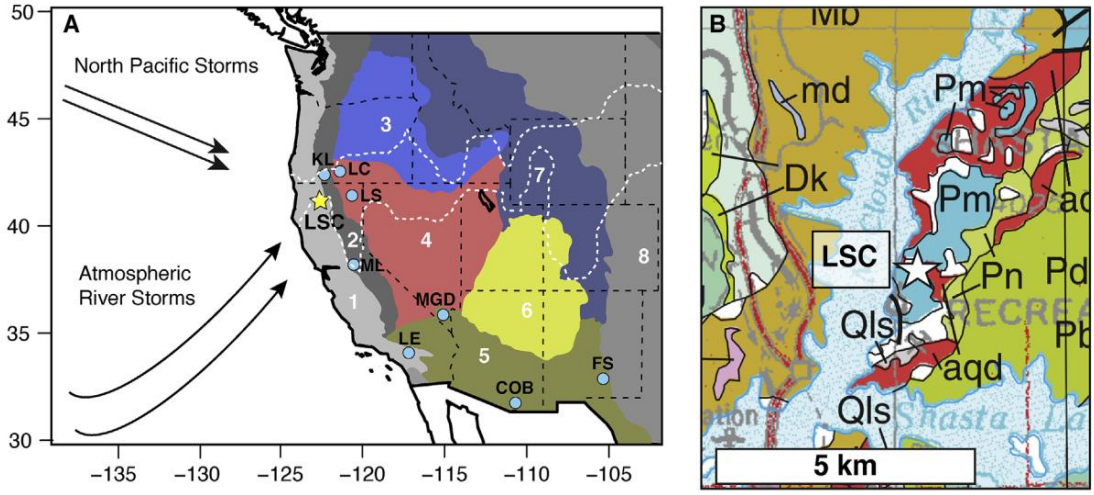

Figure 1.Location of LSC (star). Background map shows western U.S. geographic regions 1. Pacific Border; 2. Cascade-Sierra Mountains; 3. Columbia Plateau; 4. Great Basin; 5. Desert Southwest; 6. Colorado Plateau; 7. Rocky Mountains; 8. Great Plains. Light blue circles show location of proxy records discussed in the text: 1. LC= Summer Lake/Lake Chewaucan (Zic et al., 2002; Hudson et al., 2019); LS = Lake Surprise (Ibarra et al., 2014; Egger et al., 2018); MGD = Mojave groundwater deposits (Springer et al., 2015); KL= Klamath Lake (Bradbury et al., 2004); LE = Lake Elsinore (Feakins et al., 2019); COB = Cave of the Bells (Wagner et al., 2010); FS =Fort Stanton Cave (Asmerom et al., 2010, 2017); ML = McLean's Cave (Oster et al., 2015b). White dashed lines mark the approximate location of the transition zone in the precipitation dipole of (Wise, 2010), characterized by positive (northern) and negative (southern) correlations between modern winter precipitation and the Southern Oscillation Index. B) Geologic map of Lake Shasta area (LSC shown by star) (Fraticelli et al., 2012).

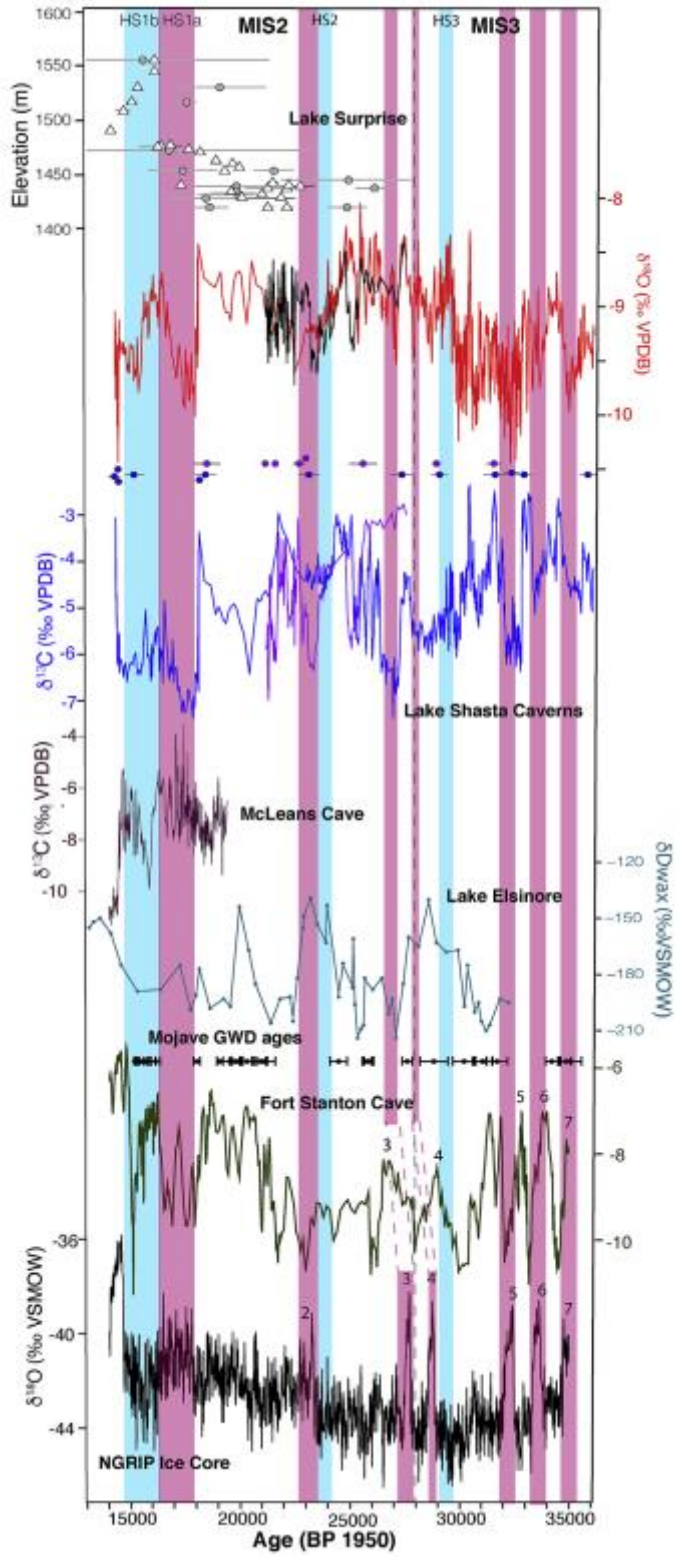

Figure 2. From top to bottom: Lake Surprise, CA lake level elevation, circles: U-series ages uncertainties (Ibarra et al., 2014), triangles ^{14}C ages (Egger et al., 2018; Ibarra et al., 2014) all uncertainties 2s; LSC $\delta^{18}O$ for LSC3 (red) and LSC2 (black); LSC $\delta^{13}C$ for LSC3 (blue) and LSC2 (purple), U-series ages and 2s uncertainties for LSC stalagmites are shown above the $\delta^{13}C$ curves; McLean's Cave $\delta^{13}C$ (Oster et al., 2015b); Lake Elsinore leaf wax δD (Feakins et al., 2019); Ages and 2 s uncertainties for Mojave groundwater deposits (black) (Springer et al., 2015); Fort Stanton Cave $\delta^{18}O$ (green) (Asmerom et al.,

2010); and NGRIP Greenland Ice Core $\delta^{18}O$ (black) (Svensson et al., 2008). D-O interstadials are numbered for NGRIP and Fort Stanton according to original publications. Heinrich Events are noted as in Fig. 5. Pink bars highlight the duration of aridisol/erosion events in the Mojave Desert (Springer et al., 2015). (For interpretation of the references to color in this figure legend, the reader is referred to the Web version of this article.)

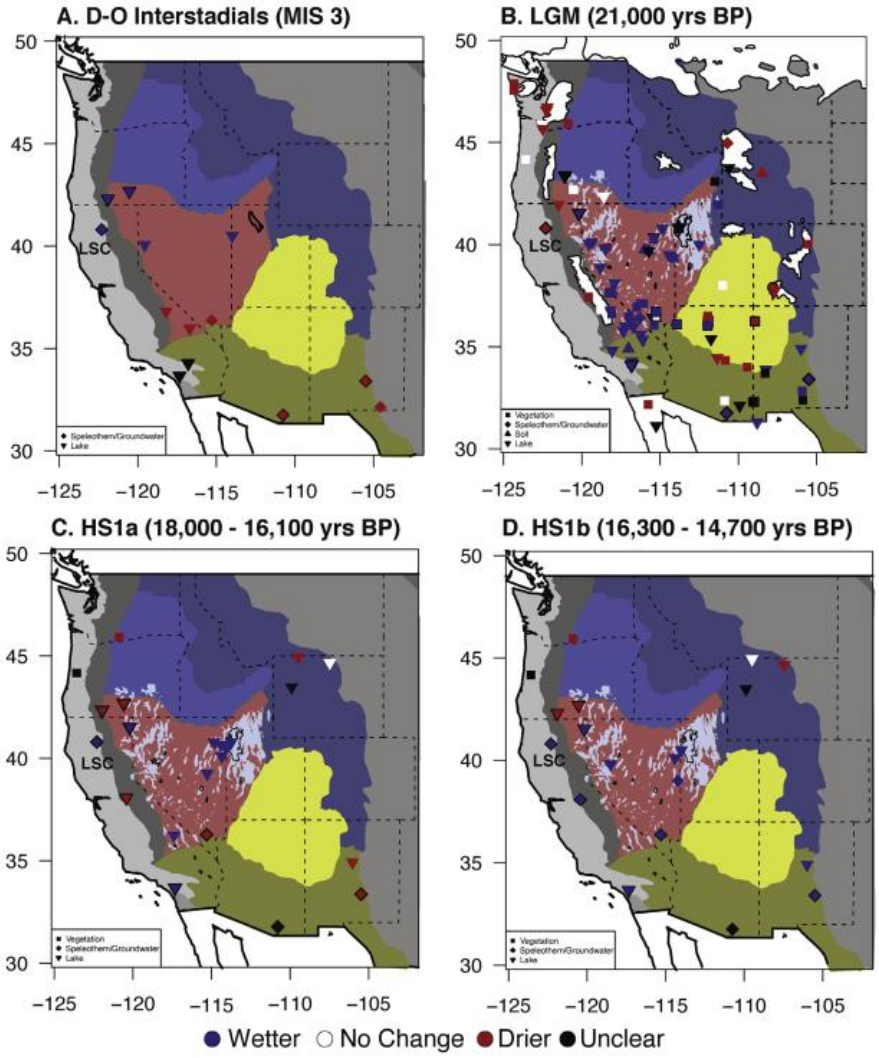

Figure 3. Spatial comparison of hydrologic conditions during (A) D-O interstadials of MIS3; (B) the LGM; (C) HS1a (18,000-16,300 yrs BP); and (D) HS1b (16,300-15,000 yrs BP).Symbol color: wet (blue); dry (red); no change relative to the reference period (white), and unclear (black). For (A), hydroclimate response is assessed relative to mean MIS3 proxy values. The LGM proxy network (B), from Oster and Ibarra (2019), is assessed relative to the modern, or the Holocene for speleothem records (diamonds) that do not extend to the present. For speleothem records in (C) and (D), hydroclimate is assessed relative to the LGM. Proxies that directly assess water balance are given priority over $\delta^{18}O$, when available. For lake records (inverted triangles) an assessment of "wet" is given if the lake level was at its highstand or has been shown to have been rising during intervals (B), (C), and (D). For (A), lake record assessments are based on proxy evidence. Background maps show geographic regions as given in Fig. 1A. Records with bold, black outlines are shown on Fig. 1A. Proxy records included in (A), (C), and (D) are listed in Table S2. (For interpretation of the references to color in this figure legend, the reader is referred to the Web version of this article.)

9. 晚白垩世(塞诺曼尼亚)西部内陆航道火山灰对初级生产力的铁施肥作用

翻译人：王敦繁
dunfan-w@foxmail.com

Zeng Z, Pike M, Tice M M, et al. ***Iron fertilization of primary productivity by volcanic ash in the Late Cretaceous (Cenomanian) Western Interior Seaway[J]. Geology,*** *2018, 46(10).*

https://doi.org/10.1130/G45304.1

摘要：火山灰含有 1%-10%的 FeO，可能是海洋表面 Fe 的重要贡献者。在过去，火山灰的铁施肥可能对海洋生产力有所贡献。本文用 x 射线荧光光谱扫描了美国德克萨斯州的含火山灰的岩心，以测试火山灰沉积和埋藏铁以及其他与生物生产力有关的微量元素之间的相关性。灰岩和页岩混合层比层间黑色页岩的铁、钼含量高，说明铁施肥促进了富锌效应(钼含量升高，铬含量降低)。此外，在火山灰沉积后的深水类群中，有孔虫组合显著减少。在缺氧条件下，含铁火山灰使塞纳曼尼亚南部西部内陆海路肥沃，促进了大量黑色页岩的沉积。

ABSTRACT： Volcanic ash contains 1%–10% FeO by weight and can be a significant contributor of Fe to the surface ocean. Fe fertilization by volcanic ash may have contributed to marine productivity in the past. A continuous core containing ash beds from the Eagle Ford Group (Texas, USA) was scanned by X-ray fluorescence spectroscopy to test for correlations between ash deposition and burial of Fe and other trace elements associated with biological productivity. Beds composed of mixed ash and shale contain much more Fe and Mo than inter- bedded black shales, implying that Fe fertilization promoted euxinia (elevated Mo and lower Cr). Moreover, foraminiferal assemblages were significantly depleted in deeper-water taxa following ash deposition. We conclude that Fe-bearing volcanic ash fertilized the southern Cenomanian Western Interior Seaway and promoted deposition of abundant black shales under anoxic conditions.

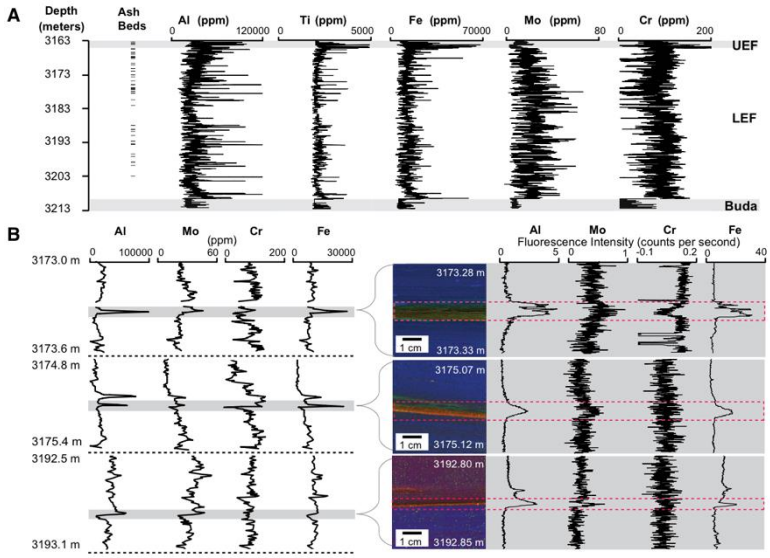

Figure1: Ash beds and elemental abundances in the Eagle Ford Group (Texas, USA). A: An abrupt decrease in Mo abundance distinguishes the Lower Eagle Ford Group (LEF) from the Buda Formation and the Upper Eagle Ford Group (UEF). Visually identified ash beds are located in the LEF and UEF. B: High-resolution (μXRF scan) compositional variation in ash beds and associated rocks from the LEF (right panel). False-color image in center of figure shows relative fluorescence intensities of Fe (red), S (green), and Ca (blue).

10. 近来磁通量延伸引起的北磁极向西伯利亚地区的快速移动

翻译人：王浩森 502691781@qq.com

Livermore P W, Finlay C C, Bayliff M ***2020. Recent north magnetic pole acceleration towards Siberia caused by flux lobe elongation. Nature Geoscience [J], 13: 387-391.***
https://doi.org/10.1038/s41561-020-0570-9

摘要：长期以来，人们一直在研究地球的北磁极，即磁场垂直指向下方的位置。自从 1831 年首次在加拿大北极地区进行实地测量以来，该极点就不断的向西伯利亚漂移，在 1990 年至 2005 年之间从其历史速度 0-15 km/yr 直到目前的 50-60 km/yr。 2017 年 10 月下旬，北磁极越过国际日期变更线，经过地理极的 390 公里以内，目前正在向南移动。本文研究指出，在过去的二十年中，北磁极的位置在很大程度上取决于加拿大和西伯利亚下方核幔边界上两个大的负磁通量凸角。模型显示，加拿大磁通量的伸长可能是由于 1970 年至 1999 年之间的地核流模式发生了变化，从而大大削弱了其在地球表面的标志性作用，导致磁极加速向西伯利亚的移动。捕获该过程的一系列简单模型表明，在未来十年中，北磁极将继续其当前轨迹，向西伯利亚再行进 390-660 公里。

ABSTRACT: The wandering of Earth's north magnetic pole, the location where the magnetic field points vertically downwards, has long been a topic of scientific fascination. Since the first in situ measurements in 1831 of its location in the Canadian arctic, the pole has drifted inexorably towards Siberia, accelerating between 1990 and 2005 from its historic speed of 0–15 km yr^{-1} to its present speed of 50–60 km yr^{-1}. In late October 2017 the north magnetic pole crossed the international date line, passing within 390 km of the geographic pole, and is now moving southwards. Here we show that over the last two decades the position of the north magnetic pole has been largely determined by two large-scale lobes of negative magnetic flux on the core–mantle boundary under Canada and Siberia. Localized modelling shows that elongation of the Canadian lobe, probably caused by an alteration in the pattern of core flow between 1970 and 1999, substantially weakened its signature on Earth's surface, causing the pole to accelerate towards Siberia. A range of simple models that capture this process indicate that over the next decade the north magnetic pole will continue on its current trajectory, travelling a further 390–660 km towards Siberia.

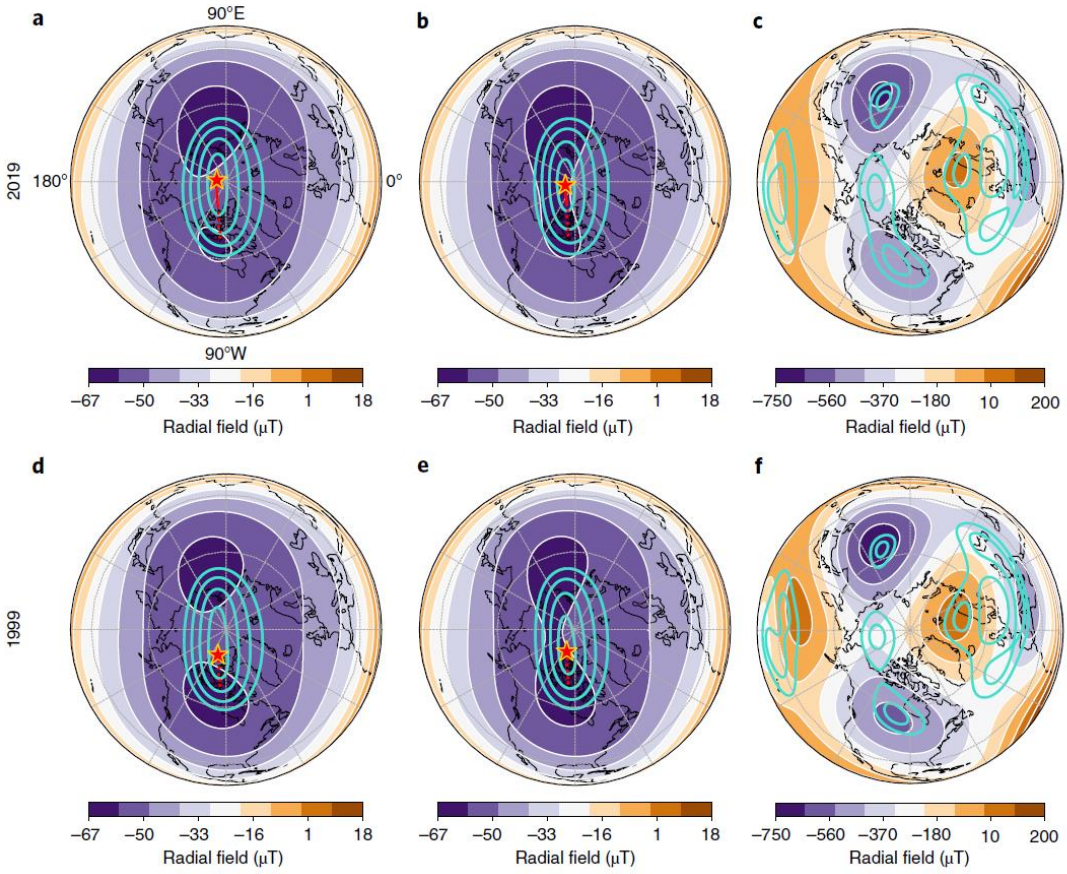

Fig. 1 | A comparison of the structure of the geomagnetic field and the north magnetic pole position in orthographic projection between 2019 and 1999. a,d, Contours of the radial field on Earth' s surface overlaid with contours of *H* in turquoise (values 2, 4, 6, 8 μT) and the north magnetic pole as a red star with a dotted tail showing the path 1840–1999, solid tail 1999–2019. b,e, As a,d but truncated to spherical-harmonic degree 6. c,f, Structure of the geomagnetic field to degree 6 on the CMB, shown by contours of radial field overlaid with contours of *H* in turquoise (values 50, 100 μT). In each panel lines of constant latitude and longitude are marked every 30°.

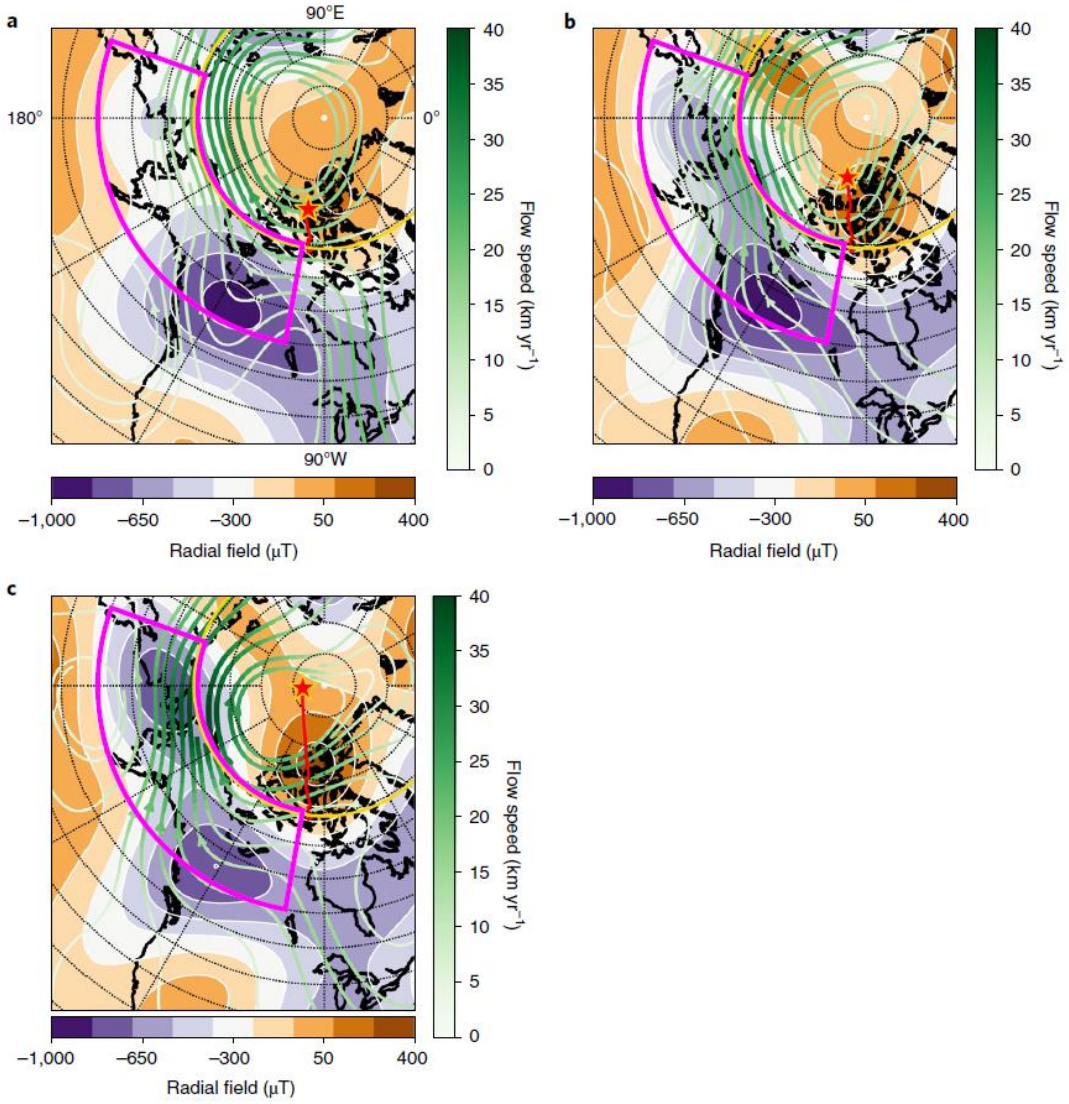

Fig. 2 | Local core surface dynamics around the Canadian flux lobe in stereographic projection. a–c, Contours of the radial magnetic field, the north magnetic pole position and path since 1840, flow streamlines with arrows and the wedge within which flux lobe elongation occurs in 1970 (a), 1999 (b) and 2017 (c). The 1970 magnetic field and flow data are from COV-OBS.x1 and the ensemble mean flow of refs. 19,21; those from 1999 are from CHAOS-6-x8 and the ensemble mean flow of refs. 19,21; those from 2017 are from CHAOS-6-x8 and the ensemble mean of refs. 20,21. The inner-core tangent cylinder is marked in gold at about 69° N. In each panel lines of constant latitude are marked every 5°.

11. 在接近封闭的体系条件下的石笋碳同位素和死碳比例：硫酸和碳酸溶解的相互作用

翻译人：郑威　11930589@mail.sustech.edu.cn

Bajo P, Borsato A, Drysdale R, et al. ***Stalagmite carbon isotopes and dead carbon proportion (DCP) in a near-closed-system situation: An interplay between sulphuric and carbonic acid dissolution****[J].* ***Geochimica et Cosmochimica Acta****, 2017, 210: 208-227.*
https://doi.org/10.1016/j.gca.2017.04.038

摘要：在本研究中，死碳比例由U-Th法和放射性碳方法计算得到，用于探索意大利Corchia洞穴沉积物的碳同位素系统。使用石笋样品（CC26）生长时间为过去12ka。CC26石笋的死碳比例为44.8-68.8%，在现有的石笋记录中最高。近乎封闭体系的条件以及硫酸溶解的共同作用被认为是造成高死碳比例的主要驱动因素，包气带深部中的陈年有机物也有微小的贡献。死碳比例和稳定碳同位素的长期衰减很可能反应了洞穴上覆的冰后期土壤，伴随着土壤二氧化碳对总溶解无机碳的贡献的逐步增加。死碳比例的显著的千年尺度变化和同期较小的不相称的稳定碳同位素变化受到作用于开放和封闭体系溶解、硫酸溶解、方解石先期沉积作用的水文变化影响。因此，Corchia洞穴沉积物的死碳比例还能够额外反映降雨量。

ABSTRACT： In this study, the ‘dead carbon proportion’ (DCP) calculated from combined U-Th and radiocarbon analyses was used to explore the carbon isotope systematics in Corchia Cave (Italy) speleothems, using the example of stalagmite CC26 which grew during the last ~12 ka. The DCP values in CC26 are among the highest ever recorded in a stalagmite, spanning the range 44.8–68.8%. A combination of almost closed-system conditions and sulphuric acid dissolution (SAD) are proposed as major drivers in producing such a high DCP with minor contribution from old organic matter from the deep vadose zone. The long-term decrease in both DCP and $\delta^{13}C$ most likely reflects post-glacial soil recovery above the cave, with a progressive increase of soil CO_2 contribution to the total dissolved inorganic carbon (DIC). Pronounced millennial-scale shifts in DCP and relatively small coeval but antipathetic changes in $\delta^{13}C$ are modulated by the effects of hydrological variability on open and closed-system dissolution, SAD and prior calcite precipitation. Hence, the DCP in Corchia Cave speleothems represents an additional proxy for rainfall amount.

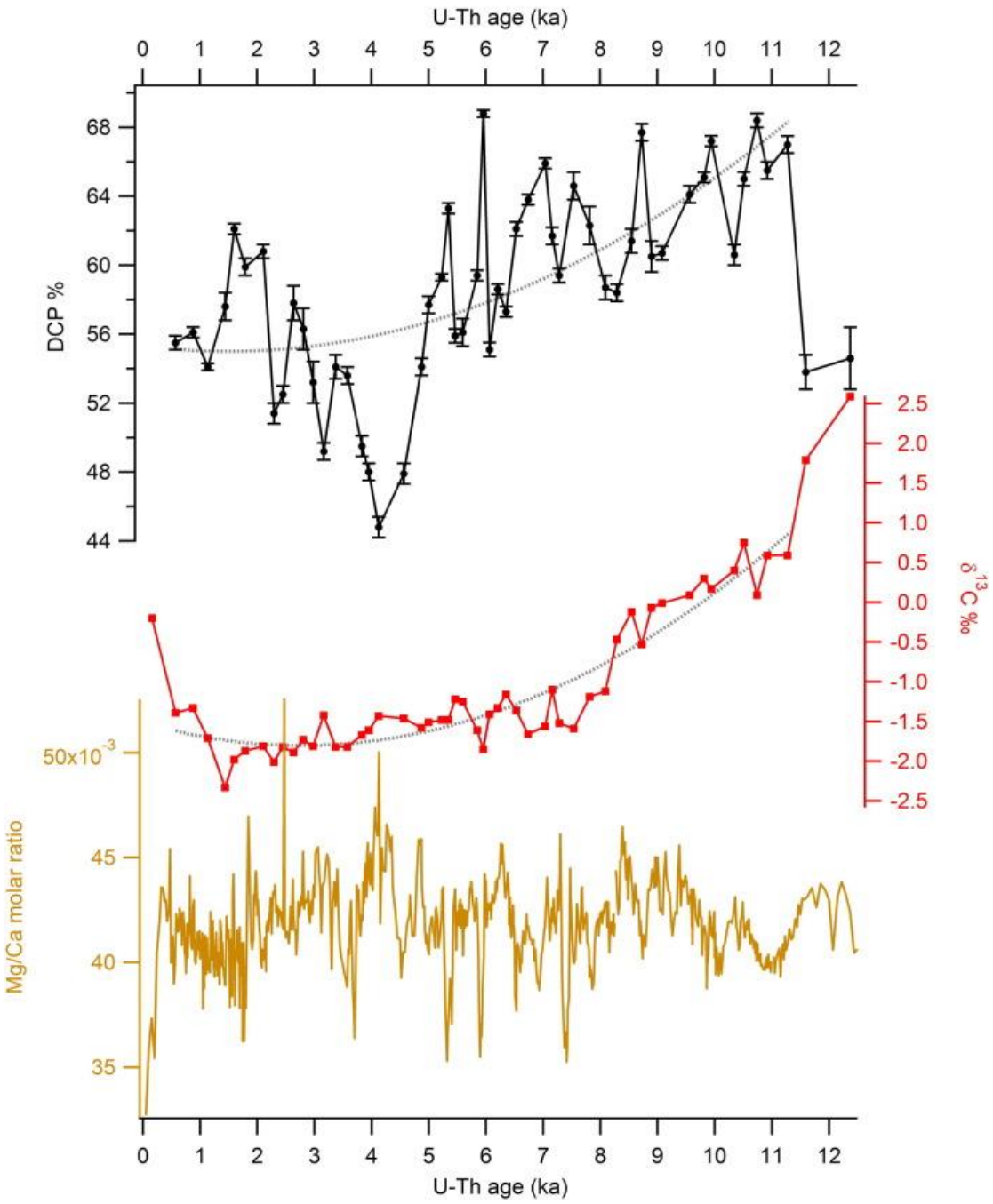

Figure 1. DCP vs $\delta^{13}C$ time series in CC26. Both DCP and $\delta^{13}C$ are high, suggesting an important contribution of C sourced from the host-rock. Dashed lines present second order polynomial fit in DCP and $\delta^{13}C$ covering the time period from 11.3 to 0.6 ka. Mg/Ca data are from Regattieri et al., 2014.